

Hidden charge order in an iron oxide square-lattice compound

Jung-Hwa Kim,^{1,*} Darren C. Peets,^{1,2,3,*} Manfred Reehuis,⁴ Peter Adler,⁵ Andrey Maljuk,^{1,6} Tobias Ritschel,³ Morgan C. Allison,³ Jochen Geck,^{3,7} Jose R. L. Mardegan,⁸ Pablo J. Bereciartua Perez,⁸ Sonia Francoual,⁸ Andrew C. Walters,^{1,9} Thomas Keller,^{1,10} Paula M. Abdala,¹¹ Philip Pattison,^{11,12} Pinder Dosanjh,¹³ and Bernhard Keimer^{1,†}

¹Max-Planck-Institut für Festkörperforschung, D-70569 Stuttgart, Germany

²Ningbo Institute for Materials Technology and Engineering,

Chinese Academy of Sciences, Zhenhai, Ningbo, 315201 Zhejiang, China

³Institut für Festkörper- und Materialphysik, Technische Universität Dresden, D-01069 Dresden, Germany

⁴Helmholtz-Zentrum Berlin für Materialien und Energie, D-14109 Berlin, Germany

⁵Max-Planck-Institut für Chemische Physik fester Stoffe, D-01187 Dresden, Germany

⁶Leibniz Institut für Festkörper- und Werkstoffforschung, D-01171 Dresden, Germany

⁷Würzburg-Dresden Cluster of Excellence ct.qmat,

Technische Universität Dresden, 01062 Dresden, Germany

⁸Deutsches Elektronen-Synchrotron DESY, Hamburg 22603, Germany

⁹Diamond Light Source, Harwell Campus, Didcot OX11 0DE, United Kingdom

¹⁰Max Planck Society Outstation at the Heinz Maier-Leibnitz Zentrum (MLZ), D-85748 Garching, Germany

¹¹SNBL at ESRF, BP 220, F-38042 Grenoble Cedex 9, France

¹²Laboratory for Quantum Magnetism, École polytechnique fédérale

de Lausanne (EPFL), BSP-Dorigny, CH-1015 Lausanne, Switzerland

¹³Department of Physics and Astronomy, University of British Columbia, Vancouver, BC, V6T 1Z1 Canada

Since the discovery of charge disproportionation in the FeO₂ square-lattice compound Sr₃Fe₂O₇ by Mössbauer spectroscopy more than fifty years ago, the spatial ordering pattern of the disproportionated charges has remained “hidden” to conventional diffraction probes, despite numerous x-ray and neutron scattering studies. We have used neutron Larmor diffraction and Fe *K*-edge resonant x-ray scattering to demonstrate checkerboard charge order in the FeO₂ planes that vanishes at a sharp second-order phase transition upon heating above 332 K. Stacking disorder of the checkerboard pattern due to frustrated interlayer interactions broadens the corresponding superstructure reflections and greatly reduces their amplitude, thus explaining the difficulty to detect them by conventional probes. We discuss implications of these findings for research on “hidden order” in other materials.

The term “hidden order” was coined for *d*- and *f*-electron compounds that undergo a thermodynamic phase transition whose order parameter cannot be identified using conventional experimental methods [1–4]. The most prominent example is URu₂Si₂ whose hidden-order phase has confounded researchers for decades, despite numerous experimental and theoretical studies [1, 2]. A lesser known, but equally puzzling case of hidden order has been found in the FeO₂ square-lattice compound Sr₃Fe₂O₇, whose electronically active Fe sites are accessible to Mössbauer spectroscopy. As early as 1966, [5, 6] Mössbauer experiments on slightly oxygen deficient Sr₃Fe₂O₇ revealed a disproportionation of the Fe⁴⁺ ions into nominal Fe³⁺ and Fe⁵⁺ valence states around room temperature. Numerous studies since then have confirmed a sharp phase transition at $T_{\text{CO}} = 340 \pm 10$ K in stoichiometric Sr₃Fe₂O₇, but no hints of a charge-ordering transition (such as a symmetry reduction or crystallographic site splitting) have ever been identified in diffraction data [6–12]. We have combined two advanced experimental methods, neutron Larmor diffraction (NLD) [13, 14] and resonant elastic x-ray scattering (REXS) [15, 16] at the Fe *K*-absorption edge, to resolve this long-standing conundrum. Specifically, we

demonstrate checkerboard charge order in the FeO₂ layers and show that the “invisibility” of charge ordering in Sr₃Fe₂O₇ originates from frustration of the interactions between neighboring layers.

The impact of geometrical frustration on charge order has been widely investigated, beginning with the classical Verwey transition in magnetite (Fe₃O₄) [17, 18], and has recently been discussed for widely different solids ranging from metal oxides [19–21] to organic conductors [22, 23], and in diverse contexts such as electronic ferroelectricity [19, 20], superconductivity [21], quantum criticality [22], and phase-change memory applications [23].

Sr₃Fe₂O₇ can serve as a model compound for frustrated charge order, because it is chemically stoichiometric and crystallizes in a body-centered tetragonal structure with FeO₂ square-lattice bilayers (Fig. 1a). This lattice architecture is common to many materials including Sr₃Ru₂O₇, La_{2–2x}Sr_{1+2x}Mn₂O₇, and La_{2–x}Sr_xCaCu₂O_{6+δ}, which have been intensely studied in relation to quantum criticality [24], magnetoresistance [25], and superconductivity [26]. Helical magnetic order due to competing exchange interactions between the Fe ions sets in at a much lower temperature ($T_{\text{N}} = 115$ K) and does not affect T_{CO} [27]. Our crystallographic data

imply that the cooperative Jahn-Teller effect is inactive and orbital order is absent in $\text{Sr}_3\text{Fe}_2\text{O}_7$, in contrast to isoelectronic manganates such as LaMnO_3 , but similar to several rare-earth nickelates $R\text{NiO}_3$ [28].

Frustration of the Coulomb interactions among valence electrons in $\text{Sr}_3\text{Fe}_2\text{O}_7$ is caused by the body-centered stacking of FeO_2 bilayers, with each Fe located directly above or below the center of a square iron-oxide plaquette in the adjacent bilayer (Fig. 1b and e (inset)). We have found superstructure reflections indicative of checkerboard charge order in the FeO_2 layers and demonstrate that stacking disorder due to frustrated interlayer coupling suppresses their amplitude below the detection limit of standard crystallographic probes. Interlayer frustration thus holds the key to the hidden-order conundrum in $\text{Sr}_3\text{Fe}_2\text{O}_7$. Possible implications for other hidden-order materials are discussed.

High-quality single crystals of $\text{Sr}_3\text{Fe}_2\text{O}_7$ were grown by the floating-zone technique [12, 30]. In order to obtain full oxygen stoichiometry, single-crystalline rods were annealed under 5-6 kbar of oxygen pressure [29]. Specific heat data (Fig. 1c) demonstrate a second-order phase transition with a sizeable entropy release of ~ 2.7 J/mol K at $T_{\text{CO}} = 332$ K. The transition is associated with a strong upturn in the in-plane resistivity (Fig. 1d), in agreement with previous reports [11, 12]. To confirm charge ordering in our $\text{Sr}_3\text{Fe}_2\text{O}_7$ samples, we conducted Mössbauer experiments on powdered crystals. The resulting spectra (Fig. 1e) reveal two components in the paramagnetic as well as in the magnetically-ordered phases, indicating charge disproportionation of Fe^{4+} into Fe^{3+} - and Fe^{5+} -like sites below T_{CO} . (Note, however, that the high formal charge in Fe^{4+} compounds has to be understood in terms of negative charge transfer energy states, in which the excess holes and the electronic density modulation reside predominantly on the oxygen ligands [31, 32].) The area ratio of 1:1 between the two subspectra confirms full oxidation of the sample and also indicates that the single iron site in the $I4/mmm$ space group has split into two distinct sites with equal population, in agreement with prior work [5–9, 11].

Before addressing the charge-ordered phase, we used single-crystal neutron diffraction to verify the high-temperature crystal structure from which this order develops. Refinements [29] in the space group $I4/mmm$ (Fig. 1a) showed no indications of any reduction in symmetry, in agreement with previous work [6, 10]. The oxygen site bridging two adjacent FeO_2 layers refined to full occupancy as expected for stoichiometric $\text{Sr}_3\text{Fe}_2\text{O}_7$.

We now turn to the crystal structure for $T < T_{\text{CO}}$. We first note that neither our neutron diffraction data nor our high-resolution synchrotron x-ray powder pattern (Fig. 2) contained any additional primitive Bragg reflections to indicate a violation of the body-centering condition, nor any obvious splitting of peaks, in agreement with prior work that failed to detect any crystal-

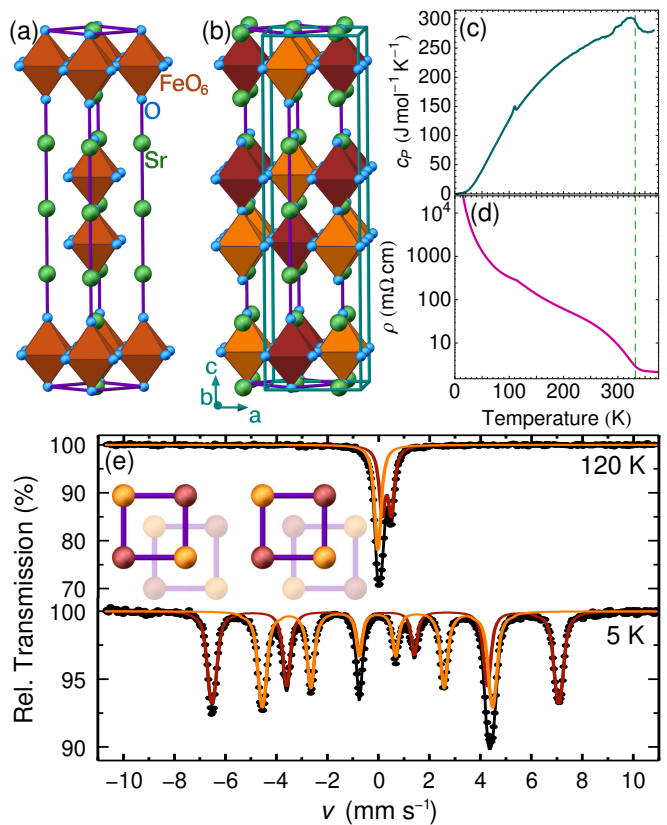


FIG. 1. Schematic crystal structures of (a) charge-disordered metallic and (b) charge-ordered insulating $\text{Sr}_3\text{Fe}_2\text{O}_7$; colors indicate the Fe valence states. (c) Specific heat. An entropy-conserving construction identifies a transition at $T_{\text{CO}} = 332$ K (dashed line), consistent with transport and diffraction data. (d) In-plane resistivity showing a metal-insulator transition at T_{CO} . The anomalies at $T \sim 115$ K in panels c and d are due to the onset of helical magnetic order. (e) Mössbauer spectra of $\text{Sr}_3\text{Fe}_2\text{O}_7$ in the paramagnetic and magnetically-ordered phases. The outer and inner components correspond to Fe^{3+} - and Fe^{5+} -like sites, respectively [6–9, 29]. Inset: Two degenerate stacking patterns of Fe^{3+} - and Fe^{5+} -like sites in adjacent bilayers.

lographic signature of charge disproportionation [6, 10]. There was a slight discrepancy between the synchrotron x-ray data and the $I4/mmm$ refinements at a handful of peaks (inset of Fig. 2). To check whether anisotropic strain below T_{CO} could explain the peak profile broadening, we used a strain model (Laue class $4/mmm$) in the refinement, but the fit did not improve substantially. Nonetheless, these deviations alone were not compelling evidence for a change in crystal symmetry.

We therefore employed neutron Larmor diffraction on the TRISP spectrometer [33] at the Maier-Leibnitz-Zentrum in Garching, Germany. NLD is capable of detecting lattice parameters d and their spread $\Delta d/d$ with a resolution better than 1×10^{-4} , independent of beam collimation and monochromaticity and of the crystal's mosaic spread [13, 14, 29]. Figure 3a shows that $\Delta d/d$

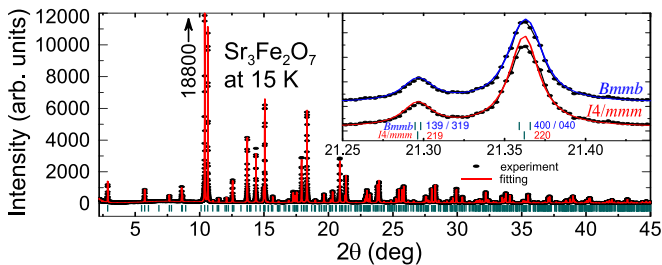


FIG. 2. High-resolution synchrotron x-ray powder diffraction pattern of the charge-ordered phase at $T = 15$ K. Inset shows the tetragonal (219) and (220) Bragg peaks, together with the results of refinements in the $I4/mmm$ and $Bmmb$ space groups.

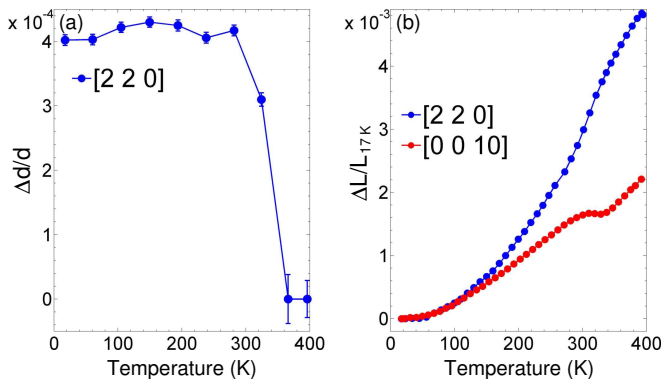


FIG. 3. Neutron Larmor diffraction results. (a) Splitting of the in-plane lattice parameters, $\Delta d/d = (b - a)/a$, extracted from the tetragonal (220) Bragg peak as a function of temperature T . In the analysis, the intrinsic peak width of $\Delta Q/Q = 4.8 \times 10^{-4}$ at 400 K was kept constant at all T . (b) Thermal expansion extracted from the cumulative Larmor phase of the tetragonal (220) and (0010) Bragg peaks, relative to the phase at $T = 17$ K.

of the tetragonal (220) Bragg reflection extracted from NLD increases sharply but continuously upon cooling below T_{CO} , then saturates at a value of 4×10^{-4} , as expected for the order parameter of a structural phase transition. No comparable change of $\Delta d/d$ is observed along the c -axis (not shown), but the thermal expansion of the c -axis parameter extracted from the Larmor phase of the (0010) reflection provides additional evidence of a continuous structural phase transition at T_{CO} (Fig. 3b).

The spread of the in-plane lattice parameters below T_{CO} revealed by NLD (Fig. 3a) and the slight discrepancy between the synchrotron x-ray data and $I4/mmm$ refinements (Fig. 2) provide clues to the lattice structure in the charge-ordered state. Based on the observation of specific superstructure reflections indicative of a unit cell with doubled in-plane area (see below), we identify the orthorhombic space group $Bmmb$ (an alternate setting of $Cmcm$, No. 63) as the simplest crystallographic description compatible with our experimental data. Here, Fe^{3+} - and Fe^{5+} -like sites in the FeO_2 planes alternate in

a checkerboard pattern within the plane and also within a bilayer unit along the c -axis [Fig. 1(b)]. The checkerboard pattern is analogous to the charge ordering patterns in the pseudocubic perovskite $CaFeO_3$, where Fe^{3+} - and Fe^{5+} -like sites alternate in all three directions [34].

Rietveld refinements in $Bmmb$ produced lattice constants $a = 5.43050(3)$ Å, $b = 5.43287(3)$ Å, and $c = 20.12134(6)$ Å. We note that the difference between a and b , $(b - a)/a = 4.0 \times 10^{-4}$, is in quantitative agreement with the independent neutron Larmor diffraction results for the in-plane $\Delta d/d$ (Fig. 3a). Complete tables of the resulting structural parameters are given in the Supplemental Materials [29]. The refinement does not indicate any rotations of the FeO_6 octahedra such as those observed in nearly-isostructural $Sr_3Ru_2O_7$ [35, 36] and in $CaFeO_3$. [34] Since substantial rotations and distortions of the FeO_6 octahedra are present in $CaFeO_3$ even above T_{CO} , the splitting of its orthorhombic Bragg reflections, $\Delta Q/Q$, is ~ 20 times that of the tetragonal peaks in $Sr_3Fe_2O_7$ for $T < T_{CO}$. Charge order then manifests as a spectral-weight shift between the split peaks, which is readily resolved by standard diffraction probes [34].

To search for weak superstructure reflections that are allowed in $Bmmb$ but not in $I4/mmm$, we first investigated a ~ 10 μ m-diameter $Sr_3Fe_2O_7$ single crystal at the BM01A beamline at the ESRF, using the wavelength 0.6973 Å. In $Bmmb$, such reflections occur at $(h, 0, l)$ for $h + k = 2n$ and $(0, k, l)$ for $l = 2n$. In $I4/mmm$, these have non-integer indices $(h/2, k/2, l)$ and are therefore forbidden. We found no intensity at the position of any superstructure reflection, and were able to place an upper bound of 10^{-5} on the ratio of the peak intensities $I(hkl) / [I(115) + I(-115)]$ (in the orthorhombic setting), which should be of order 10^{-4} according to our refinement [29]. If our space group assignment is correct, this finding implies that the superstructure reflections are broadened by disorder so that their amplitude is reduced below the detection limit.

To enhance the sensitivity to the diffraction signal from a charge modulation on the Fe sites, we performed single-crystal REXS [15, 16] measurements at the Fe K -edge (photon energy 7128 eV) at beamline P09 at PETRA-III, DESY, in Hamburg, Germany [37]. The incoming polarization was perpendicular to the scattering plane, and the outgoing polarization was not analyzed. As shown in Fig. 4, REXS indeed enables the detection of superstructure peaks at the positions predicted for the space group $Bmmb$. The $(\frac{1}{2}, \frac{1}{2}, l)$ reflections (in $I4/mmm$ notation) are direct manifestations of the unit-cell doubling due to checkerboard charge order. The intensity of the superstructure reflections decreases continuously with increasing T and vanishes at $T = T_{CO}$ (Fig. 4a). Figure 4 represents our most crucial result, as it demonstrates that the checkerboard ordering pattern is correct, and has temperature dependence consistent with Mössbauer (Fig. 1) and neutron Larmor diffraction (Fig. 3) data.

In addition to the data shown in Fig. 4, we surveyed ~ 50 reciprocal space positions, including primitive reflections forbidden in $Bmmb$ [29]. In particular, superstructure peaks having a temperature dependence consistent with those shown in Fig. 4 were also found at $(\frac{1}{2}, \frac{3}{2}, l)$ positions (tetragonal cell) for both even and odd l , but not at tetragonal $(0, 0, 2n + 1)$ or $(1, 1, 2n + 1)$, as expected for $Bmmb$. The structure factor of these reflections is roughly consistent with a model that only considers the contribution of the iron atoms resulting from the structural refinement (Fig. 4b). In this model, the structure factor of the $(\frac{1}{2}, \frac{1}{2}, l)$ reflections shown in Fig. 4b is given by $4f_1 \sin(2\pi z_1 l) + 4f_2 \sin(2\pi z_2 l)$, where $f_{1,2}$ are the form factors of inequivalent Fe ions, and $z_1 \approx -z_2 \approx 0.097$ their c -axis positions measured from the center of the unit cell (Fig. 1b center) [29]. Some deviations from the model calculations are apparent, possibly indicating a contribution from FeO_6 octahedral distortions which modulate the Fe $4p$ intermediate state of K -edge REXS, as recently found in experiments on nickel oxides [38]. Since the positional parameters of the O atoms cannot be accurately extracted from the structural refinement [29], comprehensive modelling of the REXS intensity on and off resonance goes beyond the scope of the current paper and will be the subject of future work.

Here we emphasize that the observation of the superstructure reflections and the corresponding extinction rules completes the space-group assignment in the charge-ordered state. The low-temperature space group has to accommodate iron ions in two different valence states as found by the Mössbauer experiments. Since the phase transition at T_{CO} is second order, we considered subgroups of $I4/mmm$ with two crystallographically different Fe sites. The observation of peaks at half-integer positions in h and k requires a unit cell with a doubled in-plane area. This requirement leads to $Fmmm$ and its direct subgroups. Out of these, $Cmme$ and $Cmce$ do not support charge order. $Fmmm$ itself and its subgroups $Fmm2$, $F222$, $Ccce$, and $Cccm$ can also be ruled out, because $(\frac{1}{2}, 0, l)$ and $(0, \frac{1}{2}, l)$ reflections were found for both odd and even l (Fig. 4b). Likewise, the non-observation of $(1, 1, 7)$ and $(1, 1, 9)$ (again in $I4/mmm$ notation) excludes $C2/m$. This leaves $Bmmm$ and $Bmmb$, which feature in-plane checkerboards with uniform and alternating stacking within a unit cell (and corresponding structure factors with cosine-like and sine-like dependence on l), respectively. The experimentally observed sine-like structure factor (Fig. 4b) singles out $Bmmb$, which is also favored by electrostatic and structural considerations. Deviations from orthorhombic symmetry (such as a monoclinic distortion) were not found outside the experimental uncertainty.

The REXS data yield insight into the origin of the “invisibility” of the charge-ordered state to standard diffraction probes. Whereas the width of the superstructure reflections is resolution-limited in the FeO_2 planes (which

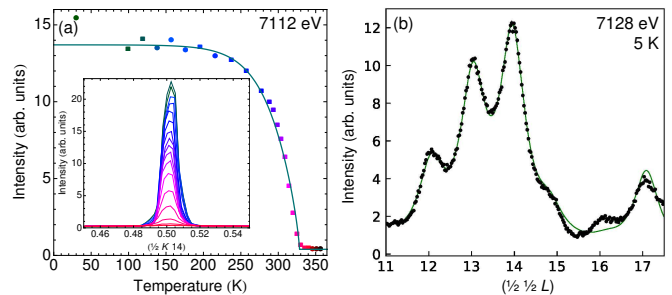


FIG. 4. (a) Temperature dependence of the integrated intensity of the $(\frac{1}{2}, \frac{1}{2}, 14)$ superstructure reflection measured by Fe K -edge REXS slightly off resonance (photon energy 7112 eV). The line is a guide to the eye. Inset: In-plane K -scans at temperatures marked by squares in the main panel, demonstrating the absence of T -dependent shifts or broadening of this reflection. (b) L -scan on resonance at $T = 30$ K. The line is the result of a calculation that considers only the Fe sites, assuming differing charge. The Fe positions were taken from the crystallographic refinement [29], and only the width, overall intensity, and the imbalance between the population of orthorhombic twin domains (45 : 55%) were fitted. Reciprocal-space locations refer to the high-temperature $I4/mmm$ cell. $(\frac{1}{2}, \frac{1}{2}, 14)$ in $I4/mmm$ is equivalent to $(1014)/(0114)$ in $Bmmb$.

implies a lower bound of ~ 100 tetragonal lattice spacings on the in-plane correlation length), the reflections are broadened into diffuse streaks along the c -axis. From their momentum width, we infer a domain size of ~ 0.65 lattice spacings along c . Because of the corresponding reduction of the peak amplitude by about two orders of magnitude, the superstructure peaks are below the detection threshold of standard neutron and non-resonant x-ray scattering. The correlation along the c -axis is strong within, but weak between bilayer units, so that the order can be regarded as quasi-two-dimensional. Nonetheless, the observation of well-defined superstructure peaks implies that the space group is correct and the stacking is not random. It is interesting to point out that the Ising symmetry of the charge order parameter allows a finite-temperature phase transition in two dimensions [39], which helps explain the sharp transition in the thermodynamic, transport, and diffraction data even in the presence of substantial stacking disorder.

The insights gained from our resolution of the long-standing $\text{Sr}_3\text{Fe}_2\text{O}_7$ conundrum provide interesting perspectives for research on hidden order in other compounds. First, we note that Mössbauer spectroscopy provides a sensitive, direct probe of the charge and spin density modulation in $\text{Sr}_3\text{Fe}_2\text{O}_7$. Without Mössbauer data (which are only obtainable on a small number of compounds with Mössbauer-active elements), the origin of the prominent phase transition in $\text{Sr}_3\text{Fe}_2\text{O}_7$ would have been far less evident. This is the case, for instance, for the layered iridates with reported hidden-order transitions [4] as well as the archetypical hidden-order com-

pound URu_2Si_2 [1, 2], which also crystallize in $I4/mmm$ with the same body-centered stacking pattern of electronically active atoms (i.e., iridium or uranium) as in $\text{Sr}_3\text{Fe}_2\text{O}_7$.

We also note that the orthorhombic distortion breaks the four-fold rotational symmetry of the tetragonal host lattice, and is thus expected to induce two-fold angular modulations in thermodynamic and transport quantities if domain averaging can be avoided (by reducing the sample volume or by applying external strain). Such modulations have indeed been identified in experiments by Okazaki and coworkers on URu_2Si_2 [40], and were attributed to “nematic” order, that is, a state with broken rotational symmetry that maintains the translational symmetry of the host lattice. Our observation of the orthorhombic supercell in $\text{Sr}_3\text{Fe}_2\text{O}_7$ suggests an alternative explanation of this behavior. The possible sensitivity of the orthorhombic domain size along the c -axis to cooling protocols or defects might help explain why the experiment of Okazaki *et al.* has been difficult to reproduce [2].

In summary, our NLD and REXS experiments have resolved the 50-year old puzzle of “hidden” charge order in $\text{Sr}_3\text{Fe}_2\text{O}_7$. The results highlight the need for further investigations of the influence of frustration and disorder on experimental observables in hidden-order phases of other materials. Finally, we point out that the high ordering temperature of $\text{Sr}_3\text{Fe}_2\text{O}_7$ might enable device applications akin to those recently proposed for organic compounds with frustrated charge order [23].

We thank an anonymous referee for insightful comments on an earlier version of this manuscript. We acknowledge funding from the Deutsche Forschungsgemeinschaft (DFG, German Research Foundation), Collaborative Research Center TRR 80 (project-ID 107745057), and through projects C03 and C06 of the Collaborative Research Center SFB 1143 (project-ID 247310070); the National Natural Science Foundation of China (Grant No. 11674367), and the Zhejiang Provincial Natural Science Foundation (Grant No. LZ18A040002). DCP is supported by the Chinese Academy of Sciences through 2018PM0036. The authors are grateful to the groups of R. Dinnebier, R. Kremer, and L. Schröder, and the staff of beamline P02.1 at PETRA-III for experimental support. We thank HZB for the allocation of neutron diffraction beamtime; DESY (Hamburg, Germany), a member of the Helmholtz Association HGF, for resonant diffraction beamtime; the European Synchrotron Radiation Facility for provision of synchrotron facilities and access to beamlines BM01A and BM01B; and the Heinz Maier-Leibnitz Zentrum (MLZ), Garching, Germany, for use of the TRISP spectrometer at FRM II.

* These authors contributed equally to this work.

† b.keimer@fkf.mpg.de

- [1] J. A. Mydosh and P. M. Oppeneer, Colloquium: Hidden order, superconductivity, and magnetism: The unsolved case of URu_2Si_2 , *Rev. Mod. Phys.* **83**, 1301 (2011), arXiv:1107.0258 [cond-mat.supr-con].
- [2] J. A. Mydosh, P. M. Oppeneer, and P. S. Riseborough, Hidden order and beyond: an experimental—theoretical overview of the multifaceted behavior of URu_2Si_2 , *Journal of Physics: Condensed Matter* **32**, 143002 (2020), arXiv:1912.09145 [cond-mat.str-el].
- [3] A. S. Cameron, G. Friemel, and D. S. Inosov, Multipolar phases and magnetically hidden order: review of the heavy-fermion compound $\text{Ce}_{1-x}\text{La}_x\text{B}_6$, *Rep. Prog. Phys.* **79**, 066502 (2016), arXiv:1509.03588 [cond-mat.str-el].
- [4] G. Cao and P. Schlottmann, The challenge of spin-orbit-tuned ground states in iridates: a key issues review, *Rep. Prog. Phys.* **81**, 042502 (2018), arXiv:1704.06007 [cond-mat.str-el].
- [5] P. K. Gallagher, J. B. MacChesney, and D. N. E. Buchanan, Mössbauer effect in the system $\text{Sr}_3\text{Fe}_2\text{O}_{6-7}$, *J. Chem. Phys.* **45**, 2466 (1966).
- [6] S. E. Dann, M. T. Weller, D. B. Currie, M. F. Thomas, and A. D. Al-Rawwas, Structure and magnetic properties of Sr_2FeO_4 and $\text{Sr}_3\text{Fe}_2\text{O}_7$ studied by powder neutron diffraction and Mössbauer spectroscopy, *J. Mater. Chem.* **3**, 1231 (1993).
- [7] P. Adler, Electronic state, magnetism, and electrical transport behavior of $\text{Sr}_{3-x}\text{A}_x\text{Fe}_2\text{O}_7$ ($x \leq 0.4$, $A = \text{Ba}, \text{La}$), *Journal of Solid State Chemistry* **130**, 129 (1997).
- [8] H. Kobayashi, M. Kira, H. Onodera, T. Suzuki, and T. Kamimura, Electronic state of $\text{Sr}_3\text{Fe}_2\text{O}_{7-y}$ studied by specific heat and Mössbauer spectroscopy, *Physica B: Condensed Matter* **237-238**, 105 (1997), proceedings of the Yamada Conference XLV, the International Conference on the Physics of Transition Metals.
- [9] P. Adler, U. Schwarz, K. Syassen, G. K. Rozenberg, G. Y. Machavariani, A. P. Milner, M. P. Pasternak, and M. Hanfland, Collapse of the charge disproportionation and covalency-driven insulator-metal transition in $\text{Sr}_3\text{Fe}_2\text{O}_7$ under pressure, *Phys. Rev. B* **60**, 4609 (1999).
- [10] K. Mori, T. Kamiyama, H. Kobayashi, S. Torii, F. Izumi, and H. Asano, Crystal structure of $\text{Sr}_3\text{Fe}_2\text{O}_{7-\delta}$, *Journal of Physics and Chemistry of Solids* **60**, 1443 (1999).
- [11] K. Kuzushita, S. Morimoto, S. Nasu, and S. Nakamura, Charge disproportionation and antiferromagnetic order of $\text{Sr}_3\text{Fe}_2\text{O}_7$, *Journal of the Physical Society of Japan* **69**, 2767 (2000).
- [12] D. C. Peets, J.-H. Kim, P. Dosanjh, M. Reehuis, A. Maljuk, N. Aliouane, C. Ulrich, and B. Keimer, Magnetic phase diagram of $\text{Sr}_3\text{Fe}_2\text{O}_{7-\delta}$, *Phys. Rev. B* **87**, 214410 (2013), arXiv:1302.1815 [cond-mat.str-el].
- [13] M. T. Rekveldt, T. Keller, and R. Golub, Larmor precession, a technique for high-sensitivity neutron diffraction, *Europhysics Letters (EPL)* **54**, 342 (2001).
- [14] T. Keller, M. T. Rekveldt, and K. Habicht, Neutron Larmor diffraction measurement of the lattice-spacing spread of pyrolytic graphite, *Appl. Phys. A* **74**, S127 (2002).
- [15] J. E. Lorenzo, Y. Joly, D. Mannix, and S. Grenier, Charge order as seen by resonant (elastic) X-ray scattering, Eu-

- rophys. J. Special Topics **208**, 121 (2012).
- [16] J. Fink, E. Schierle, E. Weschke, and J. Geck, Resonant elastic soft x-ray scattering, Reports on Progress in Physics **76**, 056502 (2013), arXiv:1210.5387 [cond-mat.mtrl-sci].
- [17] F. Walz, The Verwey transition—a topical review, Journal of Physics: Condensed Matter **14**, R285 (2002).
- [18] J. P. Attfield, Charge ordering in transition metal oxides, Solid State Sciences **8**, 861 (2006).
- [19] S. Ishihara, Electronic ferroelectricity and frustration, Journal of the Physical Society of Japan **79**, 011010 (2010), arXiv:0912.4083 [cond-mat.str-el].
- [20] N. Ikeda, T. Nagata, J. Kano, and S. Mori, Present status of the experimental aspect of $R\text{Fe}_2\text{O}_4$ study, Journal of Physics: Condensed Matter **27**, 053201 (2015).
- [21] K. Jiang, S. Zhou, and Z. Wang, Textured electronic states of the triangular-lattice Hubbard model and Na_xCoO_2 , Phys. Rev. B **90**, 165135 (2014), arXiv:1309.0518 [cond-mat.str-el].
- [22] L. Cano-Cortés, A. Ralko, C. Févriér, J. Merino, and S. Fratini, Geometrical frustration effects on charge-driven quantum phase transitions, Phys. Rev. B **84**, 155115 (2011), arXiv:1106.4408 [cond-mat.str-el].
- [23] H. Oike, F. Kagawa, N. Ogawa, A. Ueda, H. Mori, M. Kawasaki, and Y. Tokura, Phase-change memory function of correlated electrons in organic conductors, Phys. Rev. B **91**, 041101 (2015), arXiv:1501.02873 [cond-mat.str-el].
- [24] R. A. Borzi, S. A. Grigera, J. Farrell, R. S. Perry, S. J. S. Lister, S. L. Lee, D. A. Tennant, Y. Maeno, and A. P. Mackenzie, Formation of a nematic fluid at high fields in $\text{Sr}_3\text{Ru}_2\text{O}_7$, Science **315**, 214 (2007), arXiv:cond-mat/0612599 [cond-mat.str-el].
- [25] T. Kimura, Y. Tomioka, H. Kuwahara, A. Asamitsu, M. Tamura, and Y. Tokura, Interplane tunneling magnetoresistance in a layered manganite crystal, Science **274**, 1698 (1996).
- [26] R. J. Cava, B. Batlogg, R. B. van Dover, J. J. Krajewski, J. V. Waszczak, R. M. Fleming, W. F. Peck Jr, L. W. Rupp Jr, P. Marsh, A. C. W. P. James, and L. F. Schneemeyer, Superconductivity at 60 K in $\text{La}_{2-x}\text{Sr}_x\text{CaCu}_2\text{O}_6$: the simplest double-layer cuprate, Nature **345**, 602 (1990).
- [27] J.-H. Kim, A. Jain, M. Reehuis, G. Khaliullin, D. C. Peets, C. Ulrich, J. T. Park, E. Faulhaber, A. Hoser, H. C. Walker, D. T. Adroja, A. C. Walters, D. S. Inosov, A. Maljuk, and B. Keimer, Competing exchange interactions on the verge of a metal-insulator transition in the two-dimensional spiral magnet $\text{Sr}_3\text{Fe}_2\text{O}_7$, Phys. Rev. Lett. **113**, 147206 (2014), arXiv:1409.5205 [cond-mat.str-el].
- [28] I. I. Mazin, D. I. Khomskii, R. Lengsdorf, J. A. Alonso, W. G. Marshall, R. M. Ibberson, A. Podlesnyak, M. J. Martínez-Lope, and M. M. Abd-Elmeguid, Charge ordering as alternative to Jahn-Teller distortion, Phys. Rev. Lett. **98**, 176406 (2007).
- [29] See Supplemental Material in the Appendix below, including Refs. 41–46, for additional experimental details, crystallographic parameters, and Mössbauer results. CIF files of our crystal structure refinements are available as ArXiv ancillary files.
- [30] A. Maljuk, J. Stremper, C. Ulrich, M. Sofin, L. Capogna, C. Lin, and B. Keimer, Growth of $\text{Sr}_3\text{Fe}_2\text{O}_{7-x}$ single crystals by the floating zone method, Journal of Crystal Growth **273**, 207 (2004).
- [31] A. E. Bocquet, A. Fujimori, T. Mizokawa, T. Saitoh, H. Namatame, S. Suga, N. Kimizuka, Y. Takeda, and M. Takano, Electronic structure of $\text{SrFe}^{4+}\text{O}_3$ and related Fe perovskite oxides, Phys. Rev. B **45**, 1561 (1992).
- [32] R. J. Green, M. W. Haverkort, and G. A. Sawatzky, Bond disproportionation and dynamical charge fluctuations in the perovskite rare-earth nickelates, Phys. Rev. B **94**, 195127 (2016), arXiv:1608.01645 [cond-mat.str-el].
- [33] T. Keller and B. Keimer, TRISP: Three axes spin echo spectrometer, Journal of large-scale research facilities **1**, A37 (2015).
- [34] P. M. Woodward, D. E. Cox, E. Moshopoulou, A. W. Sleight, and S. Morimoto, Structural studies of charge disproportionation and magnetic order in CaFeO_3 , Phys. Rev. B **62**, 844 (2000).
- [35] H. Shaked, J. D. Jorgensen, O. Chmaissem, S. Ikeda, and Y. Maeno, Neutron diffraction study of the structural distortions in $\text{Sr}_3\text{Ru}_2\text{O}_7$, J. Solid State Chem. **154**, 361 (2000).
- [36] R. Kiyonagi, K. Tsuda, N. Aso, H. Kimura, Y. Noda, Y. Yoshida, S.-I. Ikeda, and Y. Uwatoko, Investigation of the structure of single crystal $\text{Sr}_3\text{Ru}_2\text{O}_7$ by neutron and convergent beam electron diffractions, J. Phys. Soc. Japan **73**, 639 (2004).
- [37] J. Stremper, S. Francoal, D. Reuther, D. K. Shukla, A. Skaugen, H. Schulte-Schrepping, T. Krachta, and H. Franz, Resonant scattering and diffraction beamline P09 at PETRA III, Journal of Synchrotron Radiation **20**, 541 (2013).
- [38] Y. Lu, A. Frano, M. Bluschke, M. Hepting, S. Macke, J. Stremper, P. Wochner, G. Cristiani, G. Logvenov, H.-U. Habermeier, M. W. Haverkort, B. Keimer, and E. Benckiser, Quantitative determination of bond order and lattice distortions in nickel oxide heterostructures by resonant x-ray scattering, Phys. Rev. B **93**, 165121 (2016), arXiv:1604.07317 [cond-mat.str-el].
- [39] S. Onoda, Y. Motome, and N. Nagaosa, Two-dimensional charge order in layered 2-1-4 perovskite oxides, Phys. Rev. Lett. **92**, 236403 (2004), arXiv:cond-mat/0211520 [cond-mat.stat-mech].
- [40] R. Okazaki, T. Shibauchi, H. J. Shi, Y. Haga, T. D. Matsuda, E. Yamamoto, Y. Onuki, H. Ikeda, and Y. Matsuda, Rotational symmetry breaking in the hidden-order phase of URu_2Si_2 , Science **331**, 439 (2011), arXiv:1107.5480 [cond-mat.str-el].
- [41] S. R. Hall, G. S. D. King, and J. M. Stewart, eds., *The XTAL3.4 User's Manual* (Lamb Print, University of Western Australia, Perth, 1995).
- [42] E. Prince, ed., *International Tables of Crystallography*, Vol. C (International Union of Crystallography, 2006).
- [43] J. Rodríguez-Carvajal, Recent advances in magnetic structure determination by neutron powder diffraction, Physica B: Condensed Matter **192**, 55 (1993).
- [44] Z. Klencsár, MOSSWINN—methodological advances in the field of Mössbauer data analysis, Hyperfine Interactions **217**, 117 (2013).
- [45] M. Takano, N. Nakanishi, Y. Takeda, S. Naka, and T. Takada, Charge disproportionation in CaFeO_3 studied with the Mössbauer effect, Materials Research Bulletin **12**, 923 (1977).
- [46] G. Demazeau, B. Buffat, F. Ménil, L. Fournès, M. Pouchard, J. M. Dance, P. Fabritchnyi, and P. Hagenmuller, Characterization of six-coordinated iron (V)

in an oxide lattice, Materials Research Bulletin **16**, 1465 (1981).

— Appendix: Supplemental Material —

Crystal Growth and Characterization

High-quality single crystalline rods of $\text{Sr}_3\text{Fe}_2\text{O}_7$ grown by the floating zone technique [12, 30] were annealed to full oxygen stoichiometry following two different temperature programs: The material studied here by Mössbauer spectroscopy, resistivity, neutron diffraction, Larmor diffraction, and synchrotron powder diffraction was annealed under 6 kbar of oxygen pressure at 550°C for 100 h then cooled slowly to room temperature. Crystals used for resonant x-ray diffraction and synchrotron single-crystal diffraction were annealed for 48 hours at 450°C in 5 kbar of oxygen to rapidly oxygenate the sample, cooled to 400°C in 6 hours and held there for 24 hours to ensure equilibrium, cooled to 350°C in 96 hours then to 275 in 48 hours to maximize the oxygen content, then cooled to room temperature in an additional 24 hours. Specific heat measurements were performed on both sets of samples and were indistinguishable, so these were averaged. The oxygen contents were verified by thermogravimetry, and by refinement of diffraction data. Thermogravimetric analysis indicated an oxygen content of 6.92 for the former annealing program and 6.96 for the latter, both within the uncertainty of 7.00, and additionally showed a glitch on warming at 332(5) K, consistent with the charge-order transition.

The specific heat was measured on single crystals of $\text{Sr}_3\text{Fe}_2\text{O}_7$ in a Quantum Design Physical Properties Measurement System (PPMS), in zero field and for fields up to 9 T along the c axis. No hysteresis nor field dependence was observed above the magnetic transition, and as mentioned above, measurements on crystals from the two batches were indistinguishable and were averaged. Samples were attached to the sample holder using Apiezon N grease for measurements below 200 K; Apiezon H grease was used for higher-temperature measurements to avoid the glass transition of Apiezon N grease. Resistivity was measured in standard four-probe geometry in a Quantum Design PPMS. Gold wires were attached with silver epoxy, which was allowed to cure for several hours at $180\text{--}200^\circ\text{C}$ in air before the crystal was mounted to the sample puck with GE Varnish. Thermogravimetric analysis had previously indicated that at these temperatures the oxygen mobility remains extremely low, the oxygen content does not change, and any intercalated water tends to deintercalate, ensuring that the resistivity samples were not altered or damaged while curing the epoxy.

Neutron diffraction

Single-crystal neutron diffraction was performed on the four-circle diffractometer E5 at the BER-II reactor (Helmholtz-Zentrum Berlin, Germany) using the neutron wavelength 0.896 \AA . Refinements were carried out with the program XTAL3.4 [41] using the nuclear scattering lengths $b(\text{O}) = 5.805 \text{ fm}$, $b(\text{Fe}) = 9.54 \text{ fm}$, and $b(\text{Sr}) = 7.02 \text{ fm}$ [42]. A data set of 1302 reflections (303 unique) was collected at 390 K, well above T_{CO} . Refinements of a total of 19 parameters (i.e., the overall scale and extinction factors, 4 positional parameters, and 13 anisotropic thermal parameters) in the space group $I4/mmm$ showed no indications of any reduction in symmetry. Data taken below the charge order transition showed no change.

Nonresonant x-ray diffraction

To determine the crystal structure for $T < T_{\text{CO}}$, high-resolution synchrotron powder diffraction measurements were performed at the BM01B (Swiss-Norwegian) beamline at the ESRF (Grenoble, France) using the wavelength $\lambda = 0.5035 \text{ \AA}$. The data were refined using the program FULLPROF [43], using the atomic scattering factors provided therein. However, no peak splittings or additional superstructure reflections were observed. The search for weak superstructure reflections continued at beamline BM01A at the ESRF, using a $\sim 10 \mu\text{m}$ -diameter $\text{Sr}_3\text{Fe}_2\text{O}_7$ single crystal. Data were collected with a Pilatus area detector, using the photon wavelength 0.6973 \AA .

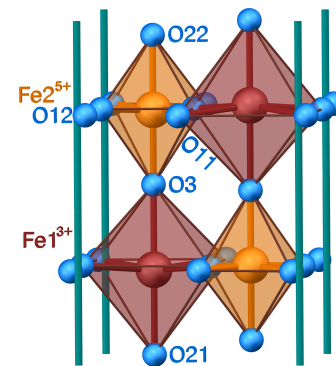


FIG. S5. Labelling of the crystallographic sites in the charge-ordered phase. The distortions are exaggerated for clarity.

Crystallographic Parameters

The atomic coordinates resulting from refinements of neutron and synchrotron x-ray diffraction data at 390 and 15 K, respectively, are shown in Tables I and II, and the Fe–O bond lengths obtained at 390 K are given in

TABLE I. Results of the crystal structure refinement of $\text{Sr}_3\text{Fe}_2\text{O}_7$ from single-crystal neutron diffraction data ($\lambda = 0.89 \text{ \AA}$) collected at 390 K. The refinement was carried out in the tetragonal space group $I4/mmm$, resulting in a residual $R_F = 0.068$. The thermal parameters U_{ij} (given in 100 \AA^2) are in the form $\exp[-2\pi^2(U_{11}h^2(a^*)^2 + \dots 2U_{13}hla^*c^*)]$. For symmetry reasons, in $I4/mmm$ the values U_{11} and U_{22} are identical for the atoms Sr1, Sr2, Fe, O1 and O3, and all parameters U_{12} , U_{13} and U_{23} are equal to zero. O1 is equatorial, O2 is apical, and O3 is the shared apical oxygen in the center of the bilayer.

Site	x	y	z	U_{11}	U_{22}	U_{33}	Occ
Sr1	$2b$	0	$0 \frac{1}{2}$	1.32(8)	1.32	1.03(8)	1
Sr2	$4e$	0	$0.31656(8)$	1.64(6)	1.64	0.97(6)	1
Fe	$4e$	0	$0.09745(6)$	0.79(4)	0.79	0.70(5)	1
O1	$8g$	$0 \frac{1}{2}$	$0.09432(8)$	1.52(8)	1.33(7)	1.23(5)	1
O2	$4e$	0	$0.19309(11)$	1.32(7)	1.32	0.99(6)	1
O3	$2a$	0	0	2.07(14)	2.07	1.64(13)	0.983(23)

$a = b = 3.846(4) \text{ \AA}$, $c = 20.234(2) \text{ \AA}$, $V = 299.4(6) \text{ \AA}^3$

TABLE II. Results of the crystal structure refinements of $\text{Sr}_3\text{Fe}_2\text{O}_7$ from high-resolution synchrotron powder diffraction data ($\lambda = 0.5035 \text{ \AA}$) collected at 15 K. The refinements were carried out in the orthorhombic space group $Bmmb$. The parameter $z(\text{O3})$ was not allowed to vary, and the thermal parameters B were constrained to be identical for each element.

$Bmmb$ Site	x	y	z	$B (\text{Å}^2)$
Sr1	$4c$	0	$\frac{3}{4}$	0.2500(12) 0.290(4)
Sr21	$4c$	0	$\frac{3}{4}$	0.4330(1) 0.290
Sr22	$4c$	0	$\frac{3}{4}$	0.0670(1) 0.290
Fe1	$4c$	0	$\frac{3}{4}$	0.6528(15) 0.306(10)
Fe2	$4c$	0	$\frac{3}{4}$	0.8471(15) 0.306
O1	$16h$	$0.248(6)$	$0.505(5)$	0.3450(1) 0.62(3)
O21	$4c$	0	$\frac{3}{4}$	0.5573(24) 0.62
O22	$4c$	0	$\frac{3}{4}$	0.9445(24) 0.62
O3	$4c$	0	$\frac{3}{4}$	0.62

$a = 5.43050(3) \text{ \AA}$, $b = 5.43287(3) \text{ \AA}$, $c = 20.12137(7) \text{ \AA}$,

Table III. Figure S5 indicates the labelling of the crystallographic sites. Somewhat enlarged standard deviations were obtained from synchrotron data for the positional parameters of the oxygen atoms in the low-temperature phase (Table II). This can be ascribed to the fact that these parameters are highly correlated, and to the fact that the scattering power of the oxygen atoms is relatively weak in x-ray diffraction.

The space group $Bmmb$ generates a general position $16h(x, y, z)$ for the equatorial O1 atoms. Here the three atomic positions could be individually refined; only the z parameter of O3 was fixed to be $z = 0.75$. Due to the enlarged standard deviations of the positional parameters

TABLE III. Fe–O bond lengths d in $\text{Sr}_3\text{Fe}_2\text{O}_7$ (in Å) at 390 K, including the average bond length d_{av} .

Sr ₃ Fe ₂ O ₇ at 390 K, in $I4/mmm$	
$d(\text{Fe-O1}) \times 4$ (eq)	1.9244(22)
$d(\text{Fe-O2}) \times 1$ (ap)	1.9352(26)
$d(\text{Fe-O3}) \times 1$ (br)	1.9718(13)
$d_{av}(\text{Fe-O})$	1.9341(21)

of the oxygen atoms, it was not possible to determine individual bond lengths $d(\text{Fe-O})$ with good accuracy. However, we have obtained reasonable averaged bond lengths $d_{av}(\text{Fe1}) = 1.950 \text{ \AA}$ and $d_{av}(\text{Fe2}) = 1.917 \text{ \AA}$.

Neutron Larmor diffraction

High-resolution neutron Larmor diffraction data were taken at the resonant spin-echo triple-axis spectrometer TRISP at the FRM-II (Garching, Germany) with neutron wavevector 2.9 \AA^{-1} . The crystal was aligned in the tetragonal (HLL) scattering plane and cooled in a closed-cycle refrigerator, and the tetragonal (220) and (0010) nuclear Bragg peaks were investigated in zero applied field. The outgoing neutron polarization was measured as a function of the magnetic field applied along the incident and scattered neutron paths, parallel to the tetragonal (220) Bragg planes. The measured polarization data for the (220) peak are shown in Fig. S6.

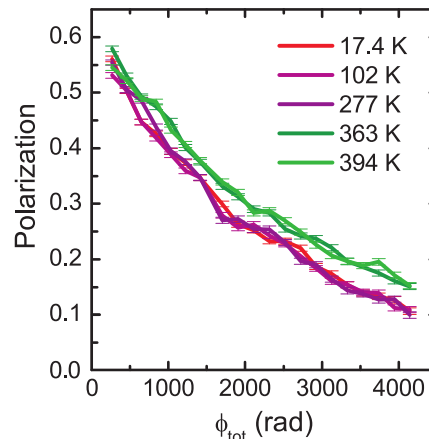


FIG. S6. Raw polarization data underpinning the neutron Larmor diffraction results on the tetragonal (220) peak. The increased depolarization at lower temperatures indicates a broadening of the lattice parameter.

Resonant elastic x-ray scattering

To enhance the contrast between the two Fe sites, we performed temperature-dependent single-crystal resonant elastic x-ray scattering (REXS) at the Fe K edge at beamline P09 at PETRA III (DESY, in Hamburg, Germany) [37], with the experimental geometry shown in the upper inset to Fig. S7(a). Before measurement, the sample was aligned using a Photonic Science Laue diffractometer with a tungsten source — the sharp diffraction spots, seen in the inset to Fig. S7(a), indicate the high quality of the single crystal. The Laue pattern produced no clear evidence for superstructure reflections. The sample was mounted on the cold finger of a closed-cycle duplex cryostat sitting in a six-circle diffractometer, with the (001) axis in the vertical scattering plane; σ polarization was used. An avalanche photodiode point detector was used to measure the scattered x-ray intensity, and a VORTEX Si-drift diode fluorescence detector was employed to measure the total fluorescence yield (TFY) from the sample. Fig. S7(a) shows the TFY of $\text{Sr}_3\text{Fe}_2\text{O}_7$ measured as a function of the incident photon energy across the Fe K edge. The main edge at around 7128 eV and a small pre-edge at around 7115 eV are clearly visible.

As can be seen in Fig. S7(b), which references peaks to the $I4/mmm$ cell, the diffraction anomalous fine structure (DAFS) of the superstructure peaks is complex. While the regular tetragonal Bragg peak (1112) shows a characteristic absorption dip at the edge, the two superstructure peaks exhibit a complex energy-dependence throughout the entire edge region. This is related to interference effects between the two Fe sites with different valences in combination with the short correlation length along the L direction. The temperature-dependent REXS data presented in the main text were collected at an energy of 7112 eV, or 1.743 Å, corresponding to the dashed vertical line in Fig. S7 just below the pre-edge features. This energy avoids the strong fluorescence background but is close enough to the edge in order to benefit from resonant enhancement. Table IV lists reciprocal-space positions probed by resonant x-ray scattering.

Mössbauer spectroscopy

Mössbauer spectra were collected between 4.8 and 316 K with a standard WissEl spectrometer, which was operated in constant-acceleration mode and was equipped with a $^{57}\text{Co}/\text{Rh}$ source. For the absorber, a crystal of $\text{Sr}_3\text{Fe}_2\text{O}_7$ was ground. The powder containing about 10 mg of natural Fe/cm² was diluted with boron nitride to ensure homogeneous distribution and filled into a Plexiglas sample container. In order to prevent sample degradation by moisture the absorber was prepared in an Ar-

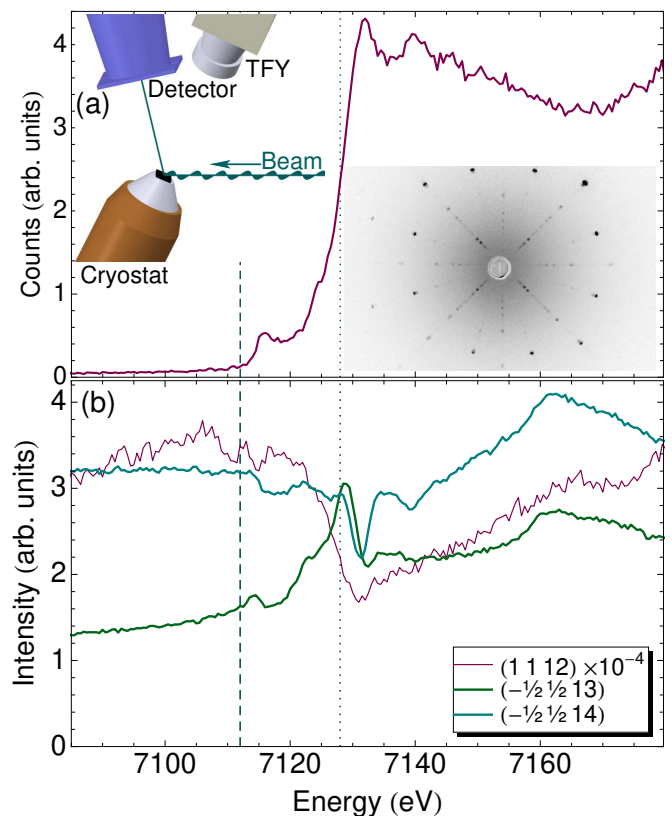


FIG. S7. (a) X-ray absorption spectrum of $\text{Sr}_3\text{Fe}_2\text{O}_7$ at the Fe K edge, from total fluorescence yield measurements. The dashed line indicates the beam energy of 7112 eV used for the temperature-dependent data in the main text while the dotted line identifies the on-resonant energy whose L -dependence is fit in Fig. 4(b). The left inset shows the experimental geometry for the $(\frac{1}{2} \frac{1}{2} 14)$ superstructure peak and for fluorescence measurements, while the right inset shows an x-ray Laue pattern of this crystal, viewed along (00 L). The incoming beam is polarized horizontally (perpendicular to the scattering plane). (b) Energy scans across the Fe K edge of two superstructure peaks and a regular Bragg peak, indexed in $I4/mmm$. The $(1112)_{I4/mmm}$ Bragg peak behaves as expected, with a significant drop in intensity at the resonance followed by a gradual recovery which is due in part to fluorescence. The superstructure peaks exhibit distinct and nontrivial energy dependence.

filled glovebox. Spectra at different temperatures were obtained using a Janis SHI-850-5 closed cycle refrigerator (CCR); the spectra at 292 and 316 K were collected with the CCR switched off. Isomer shifts are given relative to α -Fe. The data were evaluated with the program MOSSWINN [44] in the perturbation limit $QS \ll B_{hf}$, where QS corresponds to the quadrupole splitting and B_{hf} to the hyperfine field. Spectra were evaluated with Lorentzian-type sextets or with hyperfine field distributions according to the Hesse-Rübartsch method.

Representative Mössbauer spectra of $\text{Sr}_3\text{Fe}_2\text{O}_7$ in the temperature range 5-120 K are shown in Fig. S8, and the isomer shifts IS and hyperfine fields B_{hf} are depicted in

TABLE IV. List of positions probed in reciprocal space referenced to the high-temperature $I4/mmm$ unit cell, together with the peak intensity found there, normalized by incoming beam intensity. Weak peaks were also observed at positions which correspond to intergrowths of the single-layer Ruddlesden-Popper material Sr_2FeO_4 (which are common in Ruddlesden-Popper phases). From the peak intensities, we estimate that these intergrowths occur below one part in 10^4 . These peaks were verified to retain their full intensity at 330-350 K, well above the charge order transition in $\text{Sr}_3\text{Fe}_2\text{O}_7$. Based on the l -coordinate and temperature dependence, they can be discriminated from superlattice reflections that belong to $\text{Sr}_3\text{Fe}_2\text{O}_7$. However, some overlap with $\text{Sr}_3\text{Fe}_2\text{O}_7$ reflections is noted in the table. Since this experiment was intended to survey which peaks were present and was not intended to produce quantitative data, readers are cautioned against treating these numbers as quantitative. In particular, a variety of energies and temperatures were used, and some data were collected using an area detector with different sensitivity, as noted in the table. The small beam spot will lead to substantial variations in sample illumination and absorption as a function of the angle between the sample's surface normal and the beam, and, even on a single peak, variations at the 10% level routinely arise. Peak intensities measured under different conditions should not be compared, and scans along different axes should be treated with caution.

Position	Peak (counts/s)	T (K)	Axis	Energy (eV)	Notes	Position	Peak (counts/s)	T (K)	Axis	Energy (eV)	Notes
(004)	Present	5	z	7112	Area detector	(0013)	$< 8.3 \times 10^5$	5	χ	7112	overlap Sr_2FeO_4 (008)
(006)	9.5×10^{10}	5	θ	7012		(0113)	3.5×10^9	5	χ	7112	
$(\frac{1}{2} \frac{1}{2} 6)$	6.6×10^5	5	L	7112		$(\frac{1}{2} \frac{1}{2} 13)$	7.8×10^5	5	χ	7112	
$(\frac{1}{2} \frac{1}{2} 7)$	7.4×10^5	5	L	7112		$(\frac{1}{2} \frac{3}{2} 13)$	2.0×10^5	5	χ	7112	
(107)	1.8×10^8	296	θ	7112	Area detector	(1013)	4.3×10^8	5	χ	7132	
(117)	< 600	6	χ	7012		(1113)	$< 2.0 \times 10^4$	196	L	7112	overlap Sr_2FeO_4 (118)
$(\frac{1}{2} \frac{1}{2} 8)$	6.4×10^5	5	L	7112		(0013 $\frac{1}{2}$)	Absent	5	L	7112	
(118)	3.9×10^8	6	χ	7112	Area detector	(1113 $\frac{1}{2}$)	Absent	5	L	7112	
$(\frac{1}{2} \frac{1}{2} 9)$	9.2×10^5	5	L	7112		$(-\frac{1}{2} \frac{1}{2} 14)$	1.8×10^6	5	L	7117	
$(\frac{1}{2} \frac{3}{2} 9)$	1.8×10^5	5	L	7112		(0114)	Absent	5	L	7112	
(119)	< 500	6	χ	7012		$(\frac{1}{2} \frac{1}{2} 14)$	2.3×10^6	25	χ	7112	
(0010)	1.4×10^{11}	5	χ	7012		$(\frac{1}{2} \frac{3}{2} 14)$	9.0×10^5	6	χ	7112	
$(\frac{1}{2} \frac{1}{2} 10)$	1.8×10^6	5	L	7112		(1114)	2.2×10^{10}	5	L	7112	
$(\frac{1}{2} \frac{3}{2} 10)$	8.5×10^5	5	L	7112		(1114 $\frac{1}{2}$)	Absent	5	L	7112	
(1110)	2.1×10^9	296	χ	7112		$(-\frac{1}{2} \frac{1}{2} 15)$	8.6×10^5	5	χ	7112	
$(-\frac{1}{2} \frac{1}{2} 11)$	1.2×10^5	5	L	7117		(0115)	5.4×10^{10}	5	χ	7112	
$(\frac{1}{2} \frac{1}{2} 11)$	6.6×10^5	25	L	7112		$(\frac{1}{2} \frac{1}{2} 15)$	1.0×10^6	25	L	7112	
$(\frac{1}{2} \frac{3}{2} 11)$	3.5×10^5	5	L	7112		$(\frac{1}{2} \frac{3}{2} 15)$	4.1×10^5	5	L	7112	
(1111)	$< 1.5 \times 10^5$	196	L	7112	overlap Sr_2FeO_4 (117)	(0115 $\frac{1}{2}$)	Absent	5	L	7112	
$(-\frac{1}{2} \frac{1}{2} 12)$	8.3×10^4	5	L	7117		$(-\frac{1}{2} \frac{1}{2} 16)$	1.9×10^5	5	L	7080	
(0012)	2.1×10^{10}	5	χ	7012		(0116)	$< 1.0 \times 10^6$	196	L	7112	overlap Sr_2FeO_4 (0110)
(0112)	Absent	5	L	7112		$(\frac{1}{2} \frac{1}{2} 16)$	6.2×10^5	25	L	7112	
$(\frac{1}{2} \frac{1}{2} 12)$	6.2×10^3	5	χ	7012		$(\frac{1}{2} \frac{3}{2} 16)$	2.9×10^5	5	L	7112	
$(\frac{1}{2} \frac{3}{2} 12)$	9.5×10^4	5	L	7112		(0116 $\frac{1}{2}$)	Absent	197	L	7112	
(1112)	2.9×10^{10}	5	χ	7012		$(-\frac{1}{2} \frac{1}{2} 17)$	5.4×10^5	5	L	7117	
(1112 $\frac{1}{2}$)	Absent	5	L	7112		$(\frac{1}{2} \frac{1}{2} 17)$	9.1×10^5	25	L	7112	
$(-\frac{1}{2} \frac{1}{2} 13)$	8.4×10^5	5	χ	7112							

Figs. S9 and S10. The spectrum at 5 K can be described by two hyperfine sextets with distinct IS and B_{hf} values which correspond to two inequivalent iron sites. The two sextets are somewhat broadened. Since the line broadening increases with temperature, the spectra were described by two distributions of hyperfine fields, rather than by two distinct sextets with Lorentzian lineshape. The area ratio between the two subspectra is 1:1 which confirms a charge disproportionation (CD) of Fe^{4+} , in agreement with previous investigations of highly-oxidized

$\text{Sr}_3\text{Fe}_2\text{O}_7$ [6, 7, 11].

The CD is frequently written as $2\text{Fe}^{4+} \rightarrow \text{Fe}^{3+} + \text{Fe}^{5+}$. The IS and B_{hf} values are similar to those in CaFeO_3 [45] which is the classical example for a CD of Fe^{4+} . However, as pointed out previously[7], the IS of 0.31 mm/s at 5 K for the “ Fe^{3+} ” site is considerably smaller than the typical values of ~ 0.45 mm/s for Fe^{3+} in octahedral oxygen coordination, whereas the $IS = -0.03$ mm/s for “ Fe^{5+} ” is larger than for instance $IS = -0.34$ mm/s found in the Fe^{5+} double perovskite $\text{La}_2\text{FeLiO}_6$ [46]. Sim-

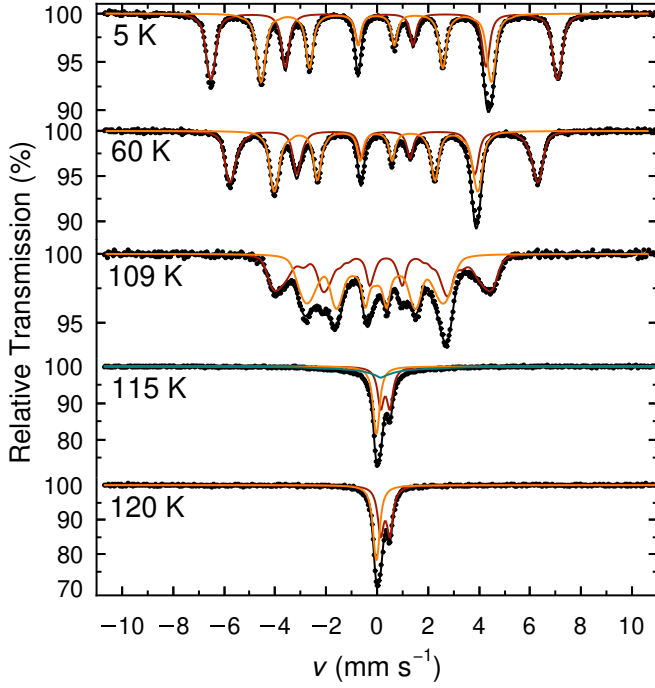


FIG. S8. Mössbauer spectra of $\text{Sr}_3\text{Fe}_2\text{O}_7$ in the magnetically-ordered phase and around the magnetic phase transition. The dark and light components correspond to the “ Fe^{3+} ” and “ Fe^{5+} ” sites, respectively. The blue component in the 115-K spectrum reflects the residual magnetically-ordered phase.

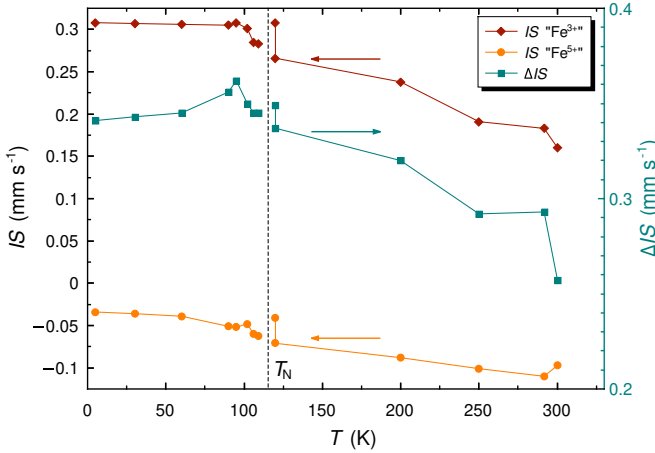


FIG. S9. Temperature dependence of the isomer shifts IS of the “ Fe^{3+} ” (dark) and “ Fe^{5+} ” (light) sites and of the difference ΔIS of the isomer shifts between the two sites (green). The solid lines are guides to the eye.

ilarly, the hyperfine fields of 42 and 28 T are smaller and larger than expected values of >50 T for Fe^{3+} and 23 T for Fe^{5+} , respectively[46]. Accordingly, the differences ΔIS and ΔB_{hf} in isomer shifts and hyperfine fields between the two species are smaller than expected for a full charge disproportionation, which is in qualitative agreement with the view that these formal iron(IV) oxides

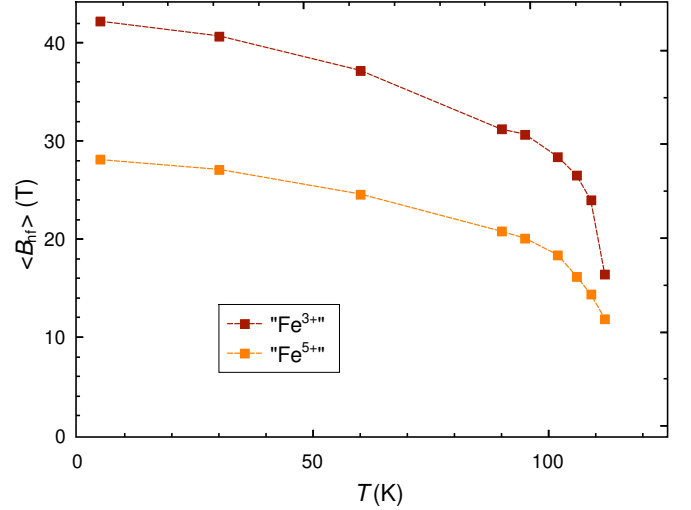


FIG. S10. Temperature dependence of the average hyperfine fields $\langle B_{hf} \rangle$ of the “ Fe^{3+} ” (dark) and “ Fe^{5+} ” (light) sites. The data were obtained by evaluation of the spectra with a distribution model. The Néel temperature was chosen to be 115.0 K, although a minor fraction is still in the magnetically ordered phase. The dashed lines are guides to the eye.

are strongly covalent and can be considered as negative- Δ materials[31], where Δ is the charge-transfer energy. Then the CD may be formulated as $2d^5L^{-1} \rightarrow d^5 + d^5L^{-2}$, where L^{-1} and L^{-2} represent one and two holes in the oxygen coordination sphere, respectively. The formulation $2\text{Fe}^{4+} \rightarrow \text{Fe}^{(4-\delta)+} + \text{Fe}^{(4+\delta)+}$ has also been used to indicate an incomplete degree of charge separation. In any case, the CD clearly alters the electron and spin densities at the iron sites which gives rise to distinct IS and B_{hf} values. As there is only a small quadrupole interaction, the different B_{hf} s correspond to different ordered magnetic moments at the two sites. For CaFeO_3 , ordered magnetic moments of 3.5 and $2.5 \mu_B$ were obtained from neutron diffraction studies for the helical state of CaFeO_3 [34]. Since the B_{hf} values of CaFeO_3 are quite similar to those of $\text{Sr}_3\text{Fe}_2\text{O}_7$, similar moments are expected. The difference ΔIS is also nearly the same in the two compounds, which implies a comparable degree of charge segregation in $\text{Sr}_3\text{Fe}_2\text{O}_7$ and CaFeO_3 .

The CD remains nearly unchanged up to the magnetic ordering temperature $T_N \sim 115$ K, where phase coexistence of the paramagnetic and magnetically-ordered phases is found. The latter appears as a broad magnetic hyperfine pattern which is superimposed on the paramagnetic subspectrum. In the magnetically-ordered phase the spectra become continuously broadened with increasing temperature which is reflected in an increased distribution width of B_{hf} . The broadening could reflect slight variations of the magnetic ordering temperature due to a residual oxygen deficiency and/or spin fluctuations. It is noteworthy that even at 5 K a broadening is observed which is more pronounced for the “ Fe^{3+} ” sub-

spectrum than for the “Fe⁵⁺” subspectrum. This may reflect the helical spin structure of Sr₃Fe₂O₇[27]. The “Fe³⁺” site has a larger quadrupole splitting than the “Fe⁵⁺” site, where the quadrupole interaction essentially vanishes. The quadrupole splitting parameter QS for “Fe³⁺” (-0.06 mm/s at 5 K) depends on the angle between the principal axis V_{ZZ} of the electric field gradient (efg) and the spin direction, which varies in the case of a helical spin structure. The resulting distribution in QS may be the origin of the increased broadening in the case of the “Fe³⁺” component.

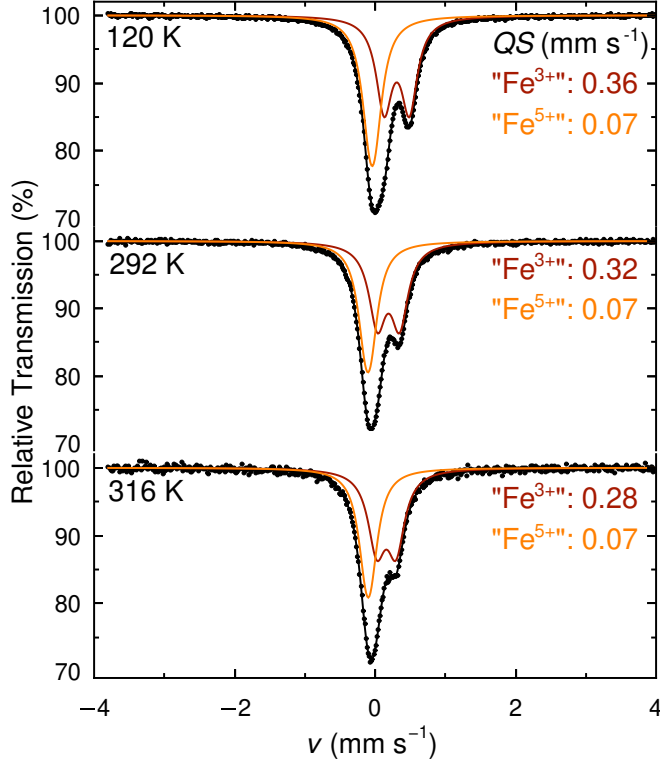


FIG. S11. Mössbauer spectra of Sr₃Fe₂O₇ in the paramagnetic phase. The dark and light components correspond to the “Fe³⁺” and “Fe⁵⁺” sites, respectively. The values QS of the quadrupole splitting are given in the figure.

At 120 K the sample is completely in the paramag-

netic state. It is obvious that the spectra between 120 and 316 K (Fig. S11) are composed of two components, which evidences that the CD persists in the paramagnetic phase. The spectra were described by two quadrupole doublets, with quadrupole splitting QS of 0.07 and 0.36 mm/s at 120 K for the “Fe⁵⁺” and “Fe³⁺” sites, respectively. Thus, the “Fe⁵⁺” component is essentially a slightly broadened single line. The temperature dependence of the isomer shifts and of the difference between the isomer shifts ΔIS of the two sites in both the magnetically ordered and the paramagnetic phase is shown in Fig. S9. In agreement with the earlier results these data suggest that the CD is largely insensitive to the magnetic phase transition. With increasing temperature, in particular above 200 K, ΔIS decreases, which indicates that the degree of charge separation is reduced[7], an effect which is also visible in the resonant diffraction results in the main text. Nevertheless, the CD is still apparent at 316 K, the highest temperature in this study. This is in agreement with the results in the main text and with the slightly higher $T_{CO} = 343 \pm 10$ K reported in Ref. 11.

We note that the fit of the spectra in the paramagnetic phase is not unique, and there is another fit with somewhat increased values of QS for both the “Fe³⁺” and the “Fe⁵⁺” sites which reproduces the spectra equally well. This data analysis, however, results in an anomaly in ΔIS near the magnetic phase transition and thus would point to a magnetostriction effect, which reduces the charge segregation at T_N . A magnetostriction effect is, however, excluded by the neutron Larmor diffraction results in the main text, and thus this fit is discarded.

In summary, the Mössbauer study on the present Sr₃Fe₂O₇ sample corroborates the CD of Fe⁴⁺ and is fully consistent with the crystal structure data at 15 K which reveal a bond-length alternation within in the double layers. The Fe1 sites with the larger bond distances correspond to the “Fe³⁺” sites in the Mössbauer spectra, whereas the Fe2 sites correspond to the contracted “Fe⁵⁺” sites.